

# Theoretical Insights into C–H Bond Activation of Methane by Transition Metal Clusters: The Role of Anharmonic Effects

Preeti Bhumla\*, Manish Kumar, and Saswata Bhattacharya\*

*Department of Physics, Indian Institute of Technology Delhi, New Delhi 110016*

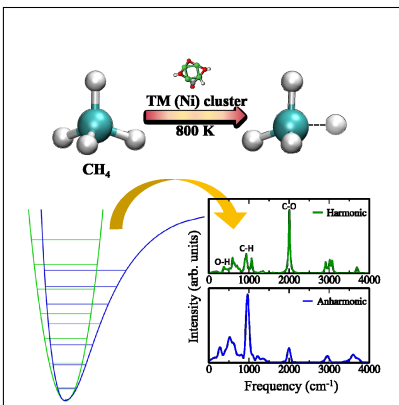
E-mail: Preeti.Bhumla@physics.iitd.ac.in[PB], saswata@physics.iitd.ac.in[SB]

Phone: +91-11-2659 1359. Fax: +91-11-2658 2037

## Abstract

Aiming towards materials design for methane activation, we study temperature ( $T$ ), pressure ( $p$ ) dependence of the composition, structure, and stability of metal oxide clusters in a reactive atmosphere using a prototypical model catalyst having wide applications: free transition metal (Ni) clusters in a combined oxygen and methane atmosphere. A robust methodological approach is employed, to show that the conventional harmonic approximation miserably fails for this class of materials and capturing anharmonic effects to the vibration free energy contribution is indispensable. To incorporate the anharmonicity in the vibrational free energy, we evaluate the excess free energy of the clusters numerically by thermodynamic integration method with hybrid density functional theory and *ab initio* molecular dynamics simulation inputs. We find that the anharmonic effect has a significant impact in detecting the activation of C–H bond, whereas the harmonic infrared spectrum completely fails due to the wrong prediction of the vibrational modes.

## Graphical TOC Entry



## Keywords

hybrid DFT, free energy, chemical potential, anharmonic effects, C–H bond activation, MD, transition metal clusters

Methane is the primary component of natural gas, which is one of the simplest, nearly ubiquitous, low-cost, clean and easily extractable energy sources found in nature.<sup>1-5</sup> Additionally, methane is also a prominent greenhouse gas. Therefore, it is highly desirable to convert methane into valuable products.<sup>6</sup> Synthesis gas (syngas, a mixture of CO and H<sub>2</sub>) production from methane is an important route for the effective utilization of abundant natural gas in producing methanol, liquid hydrocarbons, ammonia and dimethyl ether. The efficient activation of methane has been a major challenge as C–H bonds in methane possess high bond strength (4.5 eV), low polarizability and negligible electron affinity making it a least reactive hydrocarbon.<sup>7-9</sup> Since methane is extremely inert, its conversion to chemical products is difficult. To circumvent this problem, a suitable catalyst must be developed. The catalytic conversion of methane is one of the most appealing fields of study in both academia and industry.<sup>10-21</sup>

Transition metal (TM) clusters are well known for their efficient homogeneous and heterogeneous catalytic activity.<sup>22-25</sup> This is primarily ascribed to the presence of partially occupied d-shells, which assist in exhibiting multiple oxidation states in their complexes.<sup>26-28</sup> In order to understand the activity of a heterogeneous catalyst, one of the most important aspects is to identify the active species and to determine the structure of the catalyst.<sup>29</sup> Under reaction conditions, the catalyst comprises of a wide range of structures including the different number of atoms with various oxidation states, all of which could be active to some extent in the catalytic reaction. Therefore, a comprehensive understanding of the catalytic process entails a robust methodological approach that integrates various levels of theory combined into one multi-scale simulation.<sup>30</sup>

Numerous experimental and theoretical studies have established that the reactivity of small metal clusters in gas phase varies with the number of atoms.<sup>31-33</sup> It has been found that reducing particle size in the cluster reveals the possibility of several interesting size effects.<sup>28,34-36</sup> Moreover, the properties of a material change substantially under operational environment, particularly in the atmosphere of reactive molecules. Accordingly, some in-

evitable questions arise naturally, for e.g., “which are the species present in the real catalyst and what are their structures?”, and “how those catalysts change their structure and catalytic properties upon adsorption of different ligand molecules?”. In light of this, there is a justified need to provide theoretical guidance to experiments on the stoichiometry and stability of the clusters under realistic conditions. To better understand the situation theoretically, we consider a prototypical model system of nickel ( $\text{Ni}_4$ , as tetrahedron nickel cluster has high selectivity<sup>37</sup>) in a reactive atmosphere of  $\text{O}_2$  and  $\text{CH}_4$  gas molecules under realistic conditions. Note that Ni-based catalysts, owing to their low cost, high selectivity and high activity, have been extensively employed in catalysis over the past.<sup>38–40</sup> Typically, in the presence of a reactive atmosphere, clusters adsorb surrounding gas molecules and form intermediate phases  $[\text{Ni}_4\text{O}_x(\text{CH}_4)_y]$  at thermodynamic equilibrium. The latter generally proves to be an active material for various applications in the field of heterogeneous catalysis, making it crucial to have the idea of stable stoichiometries.

In this letter, we have investigated the role of environment [i.e., temperature ( $T$ ), partial pressure of oxygen ( $p_{\text{O}_2}$ ) and partial pressure of methane ( $p_{\text{CH}_4}$ )] to understand the thermodynamic stability of different configurations of  $\text{Ni}_4\text{O}_x(\text{CH}_4)_y$  ( $0 \leq x \leq 8$ ,  $0 \leq y \leq 3$ ) clusters in a reactive atmosphere of  $\text{O}_2$  and  $\text{CH}_4$  molecules. As a first step, a systematic scanning of potential energy surface (PES) is done via cascade genetic algorithm (cGA)<sup>41–43</sup> approach to obtain the global minimum (GM) configurations of  $\text{Ni}_4\text{O}_x(\text{CH}_4)_y$  clusters. Subsequently, we have employed *ab initio* atomistic thermodynamics (*aiAT*)<sup>44,45</sup> in the framework of density functional theory (DFT)<sup>46,47</sup> to determine the thermodynamic stability of those configurations under operational conditions. To incorporate the anharmonicity in the vibrational free energy contribution to the configurational entropy, we evaluate the excess free energy of the clusters numerically by thermodynamic integration method with *ab initio* molecular dynamics (*aiMD*) simulation inputs. On analyzing a large dataset, we show that the conventional harmonic approximation miserably fails to estimate the accurate thermodynamic stability. Therefore, consideration of anharmonic effects is of paramount importance to avoid all the

possibilities of missing the stable phases of the clusters. If the anharmonic effects are not included, the stable phases would be destabilized erroneously resulting in inaccurate prediction of the stable phases. Further, we have computed the Infrared (IR) spectra of these stable configurations, which also confirm the anharmonicity in such structures. Besides, the latter has significance in the activation of C–H bond, while the harmonic IR spectrum fails to capture it. The sharp peak corresponding to the C–H stretching mode (of the activated C–H bond) in the anharmonic IR spectrum signifies enhanced dipolar interaction in the C–H bond, which results from the localization of charge in C and H atoms of the  $\text{Ni}_4\text{O}_7(\text{CH}_4)_2$  cluster, is well captured by the anharmonic IR spectrum. Therefore, to develop a suitable catalyst (with active sites), incorporation of the anharmonic effects is essential in these class of materials.

After obtaining all low energy isomers corresponding to different configurations of  $\text{Ni}_4\text{O}_x(\text{CH}_4)_y$  clusters from cGA, we study their thermodynamic stability under realistic conditions using *aiAT* approach. Here, we assume that there is an exchange of atoms between the system ( $\text{Ni}_4$  cluster) and the surroundings (consisting of  $\text{O}_2$  and  $\text{CH}_4$  gas molecules) at finite temperatures and pressures, via the following reaction:



The Gibbs free energy of formation ( $\Delta G$ ) of all the  $\text{Ni}_4\text{O}_x(\text{CH}_4)_y$  structures is then evaluated as a function of  $T$ ,  $p_{\text{O}_2}$  and  $p_{\text{CH}_4}$  by applying *aiAT*. The composition (for a particular value of  $x$ ,  $y$ ) having the minimum Gibbs free energy of formation is most likely to be found in the experiments at a specific  $T$ ,  $p_{\text{O}_2}$  and  $p_{\text{CH}_4}$ .  $\Delta G(T, p)$  is, therefore, calculated as per the following equation:

$$\Delta G(T, p_{\text{O}_2}, p_{\text{CH}_4}) = F_{\text{Ni}_4\text{O}_x(\text{CH}_4)_y}(T) - F_{\text{Ni}_4}(T) - x \times \mu_{\text{O}}(T, p_{\text{O}_2}) - y \times \mu_{\text{CH}_4}(T, p_{\text{CH}_4}) \quad (2)$$

Here,  $F_{\text{Ni}_4\text{O}_x(\text{CH}_4)_y}(T)$  and  $F_{\text{Ni}_4}(T)$  are the Helmholtz free energies of the cluster+ligands

$[\text{Ni}_4\text{O}_x(\text{CH}_4)_y]$  and the pristine  $[\text{Ni}_4]$  cluster, respectively.  $x$  and  $y$  represent the number of oxygen atoms and methane molecules, that are exchanged with the environment in the reactive atmosphere, respectively.  $\mu_{\text{O}}(T, p_{\text{O}_2})$  and  $\mu_{\text{CH}_4}(T, p_{\text{CH}_4})$  represent the chemical potential of an oxygen atom ( $\mu_{\text{O}} = \frac{1}{2}\mu_{\text{O}_2}$ ) and the methane molecule, respectively. The relation of  $\mu_{\text{O}}(T, p_{\text{O}_2})$  with  $T$  and  $p_{\text{O}_2}$  is governed by the ideal (diatomic) gas approximation. The expression is as follows:<sup>48</sup>

$$\begin{aligned} \mu_{\text{O}_2}(T, p_{\text{O}_2}) = & -k_{\text{B}}T \ln \left[ \left( \frac{2\pi m}{h^2} \right)^{\frac{3}{2}} (k_{\text{B}}T)^{\frac{5}{2}} \right] \\ & + k_{\text{B}}T \ln p_{\text{O}_2} - k_{\text{B}}T \ln \left( \frac{8\pi^2 I_{\text{A}} k_{\text{B}}T}{h^2} \right) \\ & + \frac{h\nu_{\text{OO}}}{2} + k_{\text{B}}T \ln \left[ 1 - \exp \left( -\frac{h\nu_{\text{OO}}}{k_{\text{B}}T} \right) \right] \\ & + E^{\text{DFT}}(\text{O}_2) - k_{\text{B}}T \ln \mathcal{M} + k_{\text{B}}T \ln \sigma \end{aligned} \quad (3)$$

For  $\text{CH}_4$  molecule,  $I_{\text{A}}=I_{\text{B}}=I_{\text{C}}=I$ , and therefore,

$$\begin{aligned} \mu_{\text{CH}_4}(T, p_{\text{CH}_4}) = & -k_{\text{B}}T \ln \left[ \left( \frac{2\pi m}{h^2} \right)^{\frac{3}{2}} (k_{\text{B}}T)^{\frac{5}{2}} \right] \\ & + k_{\text{B}}T \ln p_{\text{CH}_4} - k_{\text{B}}T \ln \left( \frac{8\pi^2 I k_{\text{B}}T}{h^2} \right)^{\frac{3}{2}} \\ & + \frac{h\nu_{\text{CH}}}{2} + k_{\text{B}}T \ln \left[ 1 - \exp \left( -\frac{h\nu_{\text{CH}}}{k_{\text{B}}T} \right) \right] \\ & + E^{\text{DFT}}(\text{CH}_4) - k_{\text{B}}T \ln \mathcal{M} + k_{\text{B}}T \ln \sigma \end{aligned} \quad (4)$$

Here  $k_{\text{B}}$ ,  $h$ ,  $E^{\text{DFT}}$ ,  $\nu_{\text{OO}}$  and  $\nu_{\text{CH}}$  are respectively the Boltzmann constant, Planck constant, total DFT energy and stretching frequencies of O–O and C–H bonds.  $m$ ,  $I$ ,  $\mathcal{M}$  and  $\sigma$  represent the mass, moment of inertia, spin multiplicity and symmetry no. of the molecule, respectively.

The Helmholtz free energies  $F_{\text{Ni}_4\text{O}_x(\text{CH}_4)_y}(T)$  and  $F_{\text{Ni}_4}(T)$  consist of respective total DFT energy along with their free energy contributions from translational, rotational, vibrational, symmetry and spin-degeneracy terms.<sup>44</sup> It has been noticed that total DFT energy is the

dominant term, which is evaluated in its ground state configuration with respect to both geometry and spin state. The rest of the terms, except contribution from vibrational degrees of freedom ( $F_{vibs}$ ), are usually considered as invariant since they do not change much (and even if they change, the order is insignificant) due to the dependence on most of the constant terms viz. mass, moment of inertia, universal constants, etc. However, the vibrational contribution is dependent on frequencies of vibration, which are unique for a given structure. Thus, the Helmholtz free energy can be written as follows:

$$F(T) = E^{\text{DFT}} + F_{vibs} + \Delta \tag{5}$$

$\Delta$  is considered to be the constant term. At low temperature,  $F_{vibs}$  usually contributes at the first order after the decimal for a small cluster of few atoms. Thus, while computing  $\Delta G(T, p)$ , since we take differences of two free energy expressions (i.e. a system with ligands and system without ligands), we assume this to be very small and therefore, can be neglected. However, there exist some systems, where  $F_{vibs}$  contributes significantly even after taking the difference of two such terms to compute  $\Delta G(T, p)$ .<sup>45</sup> In view of this, though a significant number of works have neglected  $F_{vibs}$ , but it is not recommended. Here, we have estimated the role of  $F_{vibs}$  via state-of-the-art theoretical techniques at various level of accuracy.

Using Equation 2, we have obtained the 3D phase diagram ( $p_{\text{O}_2}$  vs  $p_{\text{CH}_4}$  vs  $\Delta G(T, p)$ ) at an experimentally relevant  $T$  (here, 800 K) by taking its 2D projection after aligning negative  $\Delta G(T, p)$  axis to be vertically up. We have considered all the configurations of  $\text{Ni}_4\text{O}_x(\text{CH}_4)_y$  clusters. Note that only those phases that minimize the  $\Delta G(T, p)$  at a specific  $p_{\text{O}_2}$ ,  $p_{\text{CH}_4}$  and  $T = 800$  K, are visible (see Figure 1). Each color in the phase diagram represents a stable configuration of the catalyst. All the phase diagrams are constructed at  $T = 800$  K as it is a suitable temperature for methane activation.

Herein, we have implemented a suite of three state-of-the-art techniques to plot  $\Delta G(T, p)$ . The first one is without any explicit contribution of  $F_{vibs}$  (as in Equation 5) i.e., only total

DFT energy ( $E^{\text{DFT}}$ ) of the cluster with and without ligands is considered (see Figure 1a). In the second case, we have duly considered  $F_{vibs}$  upto harmonic approximation to calculate  $\Delta G(T,p)$ .  $F_{vibs}^{\text{harmonic}}$  is computed using the following equation:<sup>41</sup>

$$F_{vibs}^{\text{harmonic}} = \sum_i \frac{h\nu_i}{2} + k_B T \ln \left[ 1 - \exp \left( \frac{h\nu_i}{k_B T} \right) \right] \quad (6)$$

Note that after adding  $F_{vibs}^{\text{harmonic}}$  with  $E^{\text{DFT}}$  (as in Equation 5), a new phase is introduced along with slight rearrangement of the existing phases, especially near the boundary region of competing configurations (see Figure 1b). However, despite some small changes in Figure 1a and 1b, we do not see any significant difference to identify the most stable phases at experimentally realistic pressure range. In this region,  $\text{Ni}_4\text{O}_6\text{CH}_4$ ,  $\text{Ni}_4\text{O}_7(\text{CH}_4)_2$  and  $\text{Ni}_4\text{O}_8\text{CH}_4$  are the stable phases and if we see at the region, where  $p_{\text{O}_2} = p_{\text{CH}_4} = 10^{-5}$  atm ( $T = 800$  K),  $\text{Ni}_4\text{O}_7(\text{CH}_4)_2$  comes out to be the most stable phase (see Figure 1a and 1b) irrespective of  $F_{vibs}^{\text{harmonic}}$  is taken into consideration or not. Now here, it is assumed that at  $T = 800$  K, the

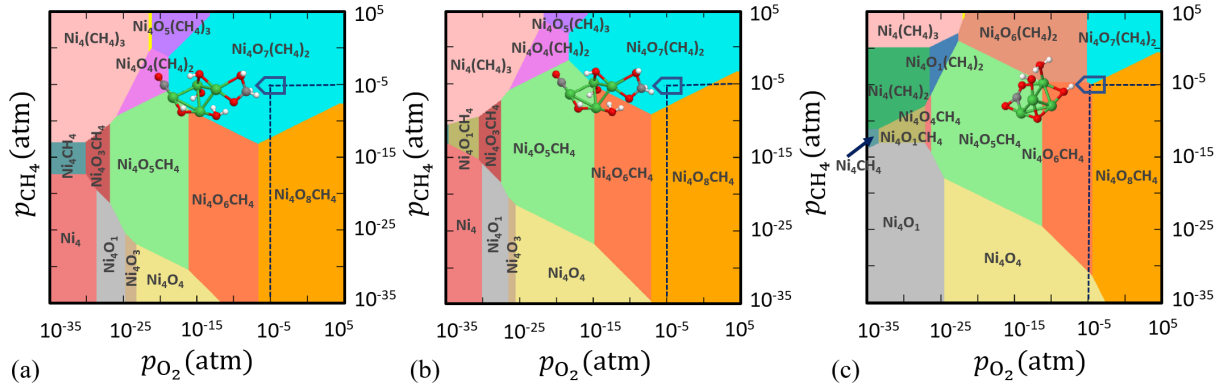


Figure 1: 2D projection of 3D phase diagram obtained for  $\text{Ni}_4\text{O}_x(\text{CH}_4)_y$  clusters in the reactive atmosphere of  $\text{O}_2$  and  $\text{CH}_4$ . In this plot  $\Delta G(T,p)$  is computed (a) when only DFT total energies are included, (b) DFT+ $F_{vibs}^{\text{harmonic}}$  are included and (c) DFT+ $F_{vibs}^{\text{anharmonic}}$  are included to compute  $F(T)$  of respective configurations as shown in Equation 2. Colored regions show the most stable compositions in a wide range of pressure at  $T = 800$  K.

oscillations are constrained to vibrate under a harmonic potential. However, the real system does not necessarily follow this assumption. And if so, the real anharmonic potential can be very different from harmonic potential. In such case, the expression for  $F_{vibs}$  can vary from



one configuration to the other.

Therefore, in an attempt to refine the expression of  $\Delta G(T, p)$  at finite  $T, p$ , we have included anharmonic effects in the potential energy surface (see Figure 1c). In order to quantitatively account for the anharmonic effects, we have performed the thermodynamic integration taking input from *aiMD* simulation to evaluate the excess free energy of clusters. Here, we have assumed that at low  $T$  (e.g. 10 K), both harmonic and anharmonic potentials do not diverge much. Taking such low  $T$  as our reference state, the Helmholtz free energy  $F(T)$  is calculated according to the following equation (for detailed derivation, see section I in Supporting Information (SI)):

$$F(T) = \underbrace{E^{\text{DFT}} + U^{\text{ZPE}}}_{U^{\text{ref}}} + \frac{T}{T_{\circ}} F_{\text{vibs}}^{\text{harmonic}}(T_{\circ}) - T \underbrace{\int_{T_{\circ}}^T \frac{dT}{T^2} (\langle U \rangle_T - U^{\text{ref}})}_{\text{thermodynamic integration}} - k_B T \frac{N}{2} \ln \frac{T}{T_{\circ}} \quad (7)$$

where  $T_{\circ}$  and  $T$  represent the initial and final temperatures, respectively.  $E^{\text{DFT}}$ ,  $U^{\text{ref}}$ ,  $F_{\text{vibs}}^{\text{harmonic}}(T_{\circ})$ ,  $N$  and  $\langle U \rangle_T$  are respectively the total DFT energy, zero point energy, Helmholtz free energy at temperature  $T_{\circ}$  (10 K) under harmonic approximation, total number of atoms and canonical average of the total energy at temperature  $T$  (800 K) of the clusters. We have run *aiMD* simulations in canonical ensemble for 8 ps at five different temperatures, from  $T = 10$  K to  $T = 800$  K to obtain the average energy ( $\langle U \rangle_T$ ). After that, we have performed quadratic curve fitting for this data and numerically integrated the corresponding function over the limits,  $T_{\circ} = 10$  K to  $T = 800$  K to get the value of  $F(T)$  at  $T = 800$  K. After evaluating  $F(T)$ , we have minimized  $\Delta G(T, p)$  using the same aforementioned procedure and obtained the phase diagram with the anharmonic effects. Interestingly, we have noticed, a completely new phase viz.  $\text{Ni}_4\text{O}_6(\text{CH}_4)_2$  appears to be stable alongside three existing phases [viz.  $\text{Ni}_4\text{O}_6\text{CH}_4$ ,  $\text{Ni}_4\text{O}_8\text{CH}_4$  and  $\text{Ni}_4\text{O}_7(\text{CH}_4)_2$ ] at reaction condition ( $p_{\text{O}_2} = p_{\text{CH}_4} = 10^{-5}$  atm and  $T = 800$  K). On comparing Figure 1a, 1b and 1c, we infer that stable phases have not only been destabilized erroneously but also the new phases have a high probability of being missed at reaction conditions, if the anharmonic effects are not taken into consideration for

this class of materials. Hence, it manifests that the inclusion of anharmonicity in these clusters affects the thermodynamic stability under operational conditions. Next, we have shown two important applications of this finding by computing the IR spectra of two test cases: (i)  $\text{Ni}_4\text{O}_6(\text{CH}_4)_2$  and (ii)  $\text{Ni}_4\text{O}_7(\text{CH}_4)_2$ .

IR spectroscopy covers the infrared region of the electromagnetic spectrum with frequencies ranging from  $4000\text{ cm}^{-1}$  to  $40\text{ cm}^{-1}$ .<sup>49–53</sup> In IR spectroscopy, specific frequencies are

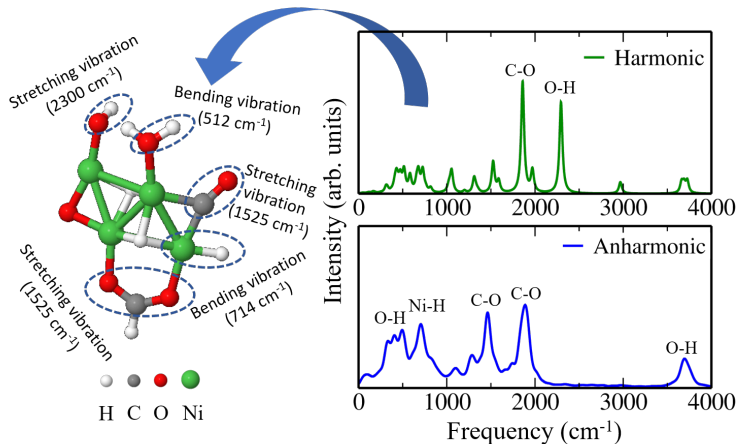


Figure 2: Infrared (IR) spectra of  $\text{Ni}_4\text{O}_6(\text{CH}_4)_2$  for both harmonic (upper panel) as well as the anharmonic (lower panel) case. The possible vibrational modes are also shown corresponding to those respective peaks.

absorbed by the molecules that are the characteristic of their structure. Here, we have simulated the IR spectra of one of the clusters viz.  $\text{Ni}_4\text{O}_6(\text{CH}_4)_2$ , that is explicitly stable on including the anharmonic contribution to the free energy, to determine its characteristic vibrational normal modes. For this, we have run 8 ps *ai*MD simulation in the canonical ensemble with Bussi-Donadio-Parrinello (BDP)<sup>54</sup> thermostat. From Figure 2, we have noticed significant dissimilarities between the harmonic and anharmonic IR spectra of  $\text{Ni}_4\text{O}_6(\text{CH}_4)_2$ . Aside from the usual difference in peak intensities, the O–H stretching mode as per harmonic IR analysis near  $2300\text{ cm}^{-1}$  (see Figure 2 upper panel) is just a negligible hump in anharmonic IR (see Figure 2 lower panel). In addition to this, there is an intense C–O bending mode visible around  $1500\text{ cm}^{-1}$ , which is not that prominent as per the harmonic analysis. Hence, it is evident that there is a fundamental difference in the characteristic

frequencies of vibration of this structure as computed with harmonic approximation and that of after capturing the anharmonic effects. As a result, they contribute differently to the free energy of vibration. This makes  $\text{Ni}_4\text{O}_6(\text{CH}_4)_2$  stable in the anharmonic case, whereas unstable under the harmonic approximation. Note that we have taken just a prototypical model system here viz.  $\text{Ni}_4$  cluster to study its stable phases under the reactive atmosphere of  $\text{O}_2$  and  $\text{CH}_4$ . Nevertheless, this model system is relevant and sufficient to convey the underlying message that there is a high chance of leaving important stable phases of the catalyst while ignoring the anharmonic effects during reaction condition.

Apart from the above important facts, we notice the additional significance of including anharmonic effects related to C–H bond activation efficiency. For this, we have considered a test case viz.  $\text{Ni}_4\text{O}_7(\text{CH}_4)_2$  cluster, which is stable in all the three cases as shown in Figure 1a, 1b and 1c. We have plotted its IR spectra (harmonic vs anharmonic) and compared in Figure 3a. From Figure 3a, we have noticed that O–H stretching presents significant anharmonic red-shifts in comparison to harmonic case around  $273\text{ cm}^{-1}$ . These red-shift corrections lead to change in IR spectrum shape due to a reorganization of the vibrational modes. Primarily, we have observed some remarkable dissimilarities between harmonic and anharmonic IR spectra, for e.g., the intensity of C–O stretching peak has reduced significantly after the inclusion of anharmonic effects. Moreover, in the anharmonic IR spectrum, we have found an intense peak around  $995\text{ cm}^{-1}$  corresponding to C–H bending vibration. This type of highly intense IR absorption is due to the change in dipole moment that occurs during a vibration, especially when the bond is highly polar in nature so that its dipole moment changes considerably as the bond stretches. Therefore, according to the anharmonic IR spectrum, this structure is supposed to be a good catalyst for C–H bond activation of methane. However, the harmonic IR spectrum completely fails to capture this information.

To validate this enhance dipolar interaction into this structure, we have plotted the charge density of  $\text{Ni}_4\text{O}_7(\text{CH}_4)_2$  cluster and compared the same with  $\text{CH}_4$  (see Figure 3b and 3c).

To obtain the charge density contour analysis, we have plotted the electron charge density

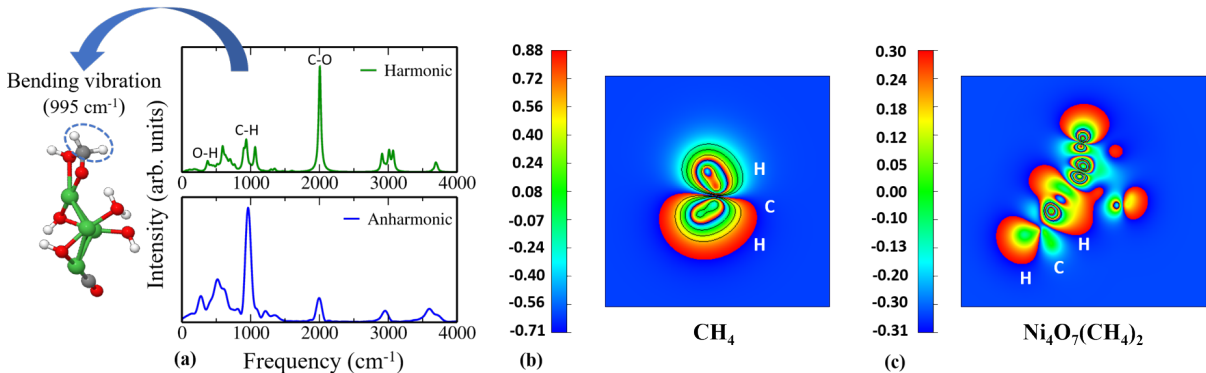


Figure 3: (a) Infrared (IR) spectra of  $\text{Ni}_4\text{O}_7(\text{CH}_4)_2$  for both harmonic as well as the anharmonic case. Contour plots of electronic charge density associated with (001) plane of (b)  $\text{CH}_4$  (delocalization of charge within C–H bonds) and (c)  $\text{Ni}_4\text{O}_7(\text{CH}_4)_2$  cluster (localization of charge within C–H bonds).

for  $\text{CH}_4$  and  $\text{Ni}_4\text{O}_7(\text{CH}_4)_2$  cluster for the electronic levels near respective Highest Occupied Molecular Orbitals (HOMO). The constant slicing plane is chosen such that both the C and H atoms of the C–H bond is covered. The value of electron charge density varies from maximum (red color) to minimum (blue color). Now, if we notice the nature of the C–H bond in either case, we can clearly see the difference in charge localization. In conventional  $\text{CH}_4$ , the C–H bond is purely covalent, which makes it rather inert to get functionalized easily. However, in the  $\text{Ni}_4\text{O}_7(\text{CH}_4)_2$  cluster, the C–H bond is very much polar with the localized charge on C and H respectively. This unusual localization of charge in the C–H bond gives rise to enhanced dipolar interactions (see Figure 3c), and as a consequence of this,  $\text{Ni}_4$  happens to be a reliable catalyst by activating the C–H bonds in methane. However, if this entire analysis is done using only harmonic approximation, this stable configuration would not even be considered for C–H bond activation as its peak in the IR spectrum is pretty small and delocalized. This further concludes the importance of capturing the anharmonic contribution to this class of materials.

In summary, we have carried out state-of-the-art hybrid density functional theory (DFT) calculations combined with *ab initio* atomistic thermodynamics (*aiAT*) and *ab initio* molec-

ular dynamics (*aiMD*) simulation to see how the thermodynamic stability of TM oxide clusters changes as a function of temperature and pressure ( $T$ ,  $p_{\text{O}_2}$  and  $p_{\text{CH}_4}$ ). While finding the accurate thermodynamic stability, we have seen that inclusion of anharmonicity introduces new stable phases that are entirely ignored by the DFT and DFT+F<sub>vibs</sub><sup>harmonic</sup>. This has a significant impact in detecting activation of C–H bond, where the harmonic IR is unable to capture the correct vibrational modes. The key point, which emerges out of these studies, is that towards understanding the activation of the stable C–H bonds in methane using a metal oxide cluster as a catalyst, capturing the anharmonic effects is essential for this class of materials.

## Methodology

We have generated a large data set of  $\text{Ni}_4\text{O}_x(\text{CH}_4)_y$  ( $0 \leq x \leq 8$ ,  $0 \leq y \leq 3$ ) clusters. We have varied the value of  $x$  and  $y$  ( $x$  = no. of oxygen atoms,  $y$  = no. of  $\text{CH}_4$  molecules) from zero to the saturation value, which means  $x$  and  $y$  values are increased with all possible combinations until no more O-atom/ $\text{CH}_4$  molecule can be absorbed by the cluster. As a first step, we have used a massively parallel cascade genetic algorithm (cGA) to thoroughly scan the potential energy surface (PES) in determining all possible low-energy structures (including the global minimum). The term “cascade” means a multi-stepped algorithm, where successive steps employ higher level of theory and each of the next level takes information obtained at its immediate lower level. Typically, a cGA algorithm starts with classical force field and goes upto density functional theory (DFT) with hybrid exchange and correlation ( $\epsilon_{xc}$ ) functionals. Note that it is reported that PBE  $\epsilon_{xc}$  functional<sup>55</sup> highly overestimates stability of clusters containing larger concentration of O-atoms.<sup>29,33,42,56</sup> This results in a qualitatively wrong prediction of  $\text{O}_2$  adsorption for O-rich cases. Such behaviour is not confirmed by more advanced hybrid  $\epsilon_{xc}$  functionals [e.g HSE06,<sup>57</sup> PBE0<sup>58</sup>] as employed in our calculations. Moreover, the spin states of the clusters are also different as found by PBE and PBE0/HSE06.

In view of this, in the cascade algorithm, we have only optimized with PBE but the energetics are computed with PBE0<sup>58</sup> to evaluate the fitness function of the cluster. For details of this cGA implementation, accuracy and validation, we recommend our previous studies as given in Ref.<sup>41–43</sup>

All DFT calculations have been performed using FHI-aims code, employing an all-electron code with numerical atom centered basis sets.<sup>59</sup> Considering the fact that first-principles based calculations are computationally demanding, lighter (viz. light settings with tier 2 basis set<sup>59</sup>) DFT settings have been implemented in the cGA to find the global minimum structures. The atomic zero-order regular approximation (ZORA) is used for the scalar relativistic correction.<sup>60</sup> The vdW correction is calculated according to the Tkatchenko-Scheffler scheme.<sup>61</sup> The low energy structures obtained from the cGA are further optimized with PBE at higher level settings (viz. tight settings with tier 2 basis set<sup>59</sup>). The atomic forces are converged up to  $10^{-5}$  eV/Å. Finally, the total single point energy is calculated on top of this optimized structure using PBE0 hybrid  $\epsilon_{xc}$  functional (see further details for validation of  $\epsilon_{xc}$  functionals as in section II in SI). The vibrational frequencies are determined of the stable compositions under harmonic approximation using finite displacement method.

Next, to capture the anharmonic effects using thermodynamic integration method, we have carried out *ab initio* molecular dynamics (MD) simulations for 8 ps each at different temperatures namely  $T = 50$  K, 100 K, 300 K, 600 K and 800 K in canonical ensemble (i.e., one with constant temperature and volume). We have employed Velocity Verlet scheme<sup>62</sup> for the integration of Newtonian equations with a time-step of 1 fs and the temperature of the system is controlled using Nose-Hoover thermostat.<sup>63</sup> (for details see section III in SI)

## Acknowledgement

PB acknowledges UGC, India, for the junior research fellowship [1392/(CSIR-UGC NET JUNE 2018)]. MK acknowledges CSIR, India, for the senior research fellowship [grant no.

09/086(1292)/2017-EMR-I]. SB acknowledges the financial support from SERB under core research grant (grant no. CRG/2019/000647). PB acknowledges Shikha Saini for helpful discussions. We acknowledge the High Performance Computing (HPC) facility at IIT Delhi for computational resources.

## Supporting Information Available

Details of choice of functionals, temperature control by Nose-Hoover thermostat and thermodynamic integration can be found in the supporting information file.

## References

- (1) Prats, H.; Gutierrez, R. A.; Pinero, J. J.; Vines, F.; Bromley, S. T.; Ramirez, P. J.; Rodriguez, J. A.; Illas, F. Room Temperature Methane Capture and Activation by Ni Clusters Supported on TiC(001): Effects of Metal–Carbide Interactions on the Cleavage of the C–H Bond. *Journal of the American Chemical Society* **2019**, *141*, 5303–5313.
- (2) Goodman, E. D.; Latimer, A. A.; Yang, A.-C.; Wu, L.; Tahsini, N.; Abild-Pedersen, F.; Cargnello, M. Low-Temperature Methane Partial Oxidation to Syngas with Modular Nanocrystal Catalysts. *ACS Applied Nano Materials* **2018**, *1*, 5258–5267.
- (3) Pal, P.; Singha, R. K.; Saha, A.; Bal, R.; Panda, A. B. Defect-Induced Efficient Partial Oxidation of Methane over Nonstoichiometric Ni/CeO<sub>2</sub> Nanocrystals. *The Journal of Physical Chemistry C* **2015**, *119*, 13610–13618.
- (4) Enger, B. C.; Lodeng, R.; Holmen, A. A review of catalytic partial oxidation of methane to synthesis gas with emphasis on reaction mechanisms over transition metal catalysts. *Applied Catalysis A: General* **2008**, *346*, 1–27.

- (5) Leenders, S. H.; Gramage-Doria, R.; de Bruin, B.; Reek, J. N. Transition metal catalysis in confined spaces. *Chemical Society Reviews* **2015**, *44*, 433–448.
- (6) Aasberg-Petersen, K.; Hansen, J.-H. B.; Christensen, T.; Dybkjaer, I.; Christensen, P. S.; Nielsen, C. S.; Madsen, S. W.; Rostrup-Nielsen, J. Technologies for large-scale gas conversion. *Applied Catalysis A: General* **2001**, *221*, 379–387.
- (7) Zhao, Y.-X.; Li, Z.-Y.; Yang, Y.; He, S.-G. Methane Activation by Gas Phase Atomic Clusters. *Accounts of Chemical Research* **2018**, *51*, 2603–2610.
- (8) Li, H.-F.; Zhao, Y.-X.; Yuan, Z.; Liu, Q.-Y.; Li, Z.-Y.; Li, X.-N.; Ning, C.-G.; He, S.-G. Methane Activation by Tantalum Carbide Cluster Anions Ta<sub>2</sub>C<sub>4</sub>. *The Journal of Physical Chemistry Letters* **2017**, *8*, 605–610.
- (9) Li, H.-F.; Li, Z.-Y.; Liu, Q.-Y.; Li, X.-N.; Zhao, Y.-X.; He, S.-G. Methane Activation by Iron-Carbide Cluster Anions FeC<sub>6</sub>. *The Journal of Physical Chemistry Letters* **2015**, *6*, 2287–2291.
- (10) Fleys, M.; Simon, Y.; Swierczynski, D.; Kiennemann, A.; Marquaire, P.-M. Investigation of the Reaction of Partial Oxidation of Methane over Ni/La<sub>2</sub>O<sub>3</sub> Catalyst. *Energy & Fuels* **2006**, *20*, 2321–2329.
- (11) Gil-Calvo, M.; Jimenez-Gonzalez, C.; de Rivas, B.; Gutierrez–Ortiz, J. I.; Lopez-Fonseca, R. Novel Nickel Aluminate-Derived Catalysts Supported on Ceria and Ceria–Zirconia for Partial Oxidation of Methane. *Industrial & Engineering Chemistry Research* **2017**, *56*, 6186–6197.
- (12) Bhavsar, S.; Vesper, G. Chemical looping beyond combustion: production of synthesis gas via chemical looping partial oxidation of methane. *RSC Adv.* **2014**, *4*, 47254–47267.
- (13) Hickman, D. A.; Schmidt, L. D. Production of Syngas by Direct Catalytic Oxidation of Methane. *Science* **1993**, *259*, 343–346.



- (14) Neumann, D.; Kirchhoff, M.; Vesper, G. Towards an efficient process for small-scale, decentralized conversion of methane to synthesis gas: combined reactor engineering and catalyst synthesis. *Catalysis Today* **2004**, *98*, 565 – 574.
- (15) Ashcroft, A.; Cheetham, A.; Foord, J. a.; Green, M.; Grey, C.; Murrell, A.; Vernon, P. Selective oxidation of methane to synthesis gas using transition metal catalysts. *Nature* **1990**, *344*, 319–321.
- (16) Vernon, P. D.; Green, M. L.; Cheetham, A. K.; Ashcroft, A. T. Partial oxidation of methane to synthesis gas. *Catalysis Letters* **1990**, *6*, 181–186.
- (17) Ramaswamy, R. C.; Ramachandran, P. A.; Dudukovic, M. P. Modeling Catalytic Partial Oxidation of Methane to Syngas in Short-Contact-Time Packed-Bed Reactors. *Industrial & Engineering Chemistry Research* **2007**, *46*, 8638–8651.
- (18) Hu, Y. H.; Ruckenstein, E. Catalyst Temperature Oscillations during Partial Oxidation of Methane. *Industrial & Engineering Chemistry Research* **1998**, *37*, 2333–2335.
- (19) Bharadwaj, S.; Schmidt, L. Catalytic partial oxidation of natural gas to syngas. *Fuel Processing Technology* **1995**, *42*, 109 – 127.
- (20) Hellman, A.; Resta, A.; Martin, N. M.; Gustafson, J.; Trincherro, A.; Carlsson, P.-A.; Balmes, O.; Felici, R.; van Rijn, R.; Frenken, J. W. M. et al. The Active Phase of Palladium during Methane Oxidation. *The Journal of Physical Chemistry Letters* **2012**, *3*, 678–682.
- (21) Hundt, P. M.; van Reijzen, M. E.; Ueta, H.; Beck, R. D. Vibrational Activation of Methane Chemisorption: The Role of Symmetry. *The Journal of Physical Chemistry Letters* **2014**, *5*, 1963–1967.
- (22) Aiken III, J. D.; Finke, R. G. A review of modern transition-metal nanoclusters: their

- synthesis, characterization, and applications in catalysis. *Journal of Molecular Catalysis A: Chemical* **1999**, *145*, 1–44.
- (23) Hill, C. L.; Prosser-McCartha, C. M. Homogeneous catalysis by transition metal oxygen anion clusters. *Coordination Chemistry Reviews* **1995**, *143*, 407–455.
- (24) Suss-Fink, G.; Meister, G. In *Transition Metal Clusters In Homogeneous Catalysis*; Stone, F., West, R., Eds.; Advances in Organometallic Chemistry; Academic Press, 1993; Vol. 35; pp 41 – 134.
- (25) Guo, H.; Sautet, P.; Alexandrova, A. N. Reagent Triggers Isomerization of Fluxional Cluster Catalyst via Dynamic Coupling. *The Journal of Physical Chemistry Letters* **0**, *0*, null.
- (26) Ruiz Puigdollers, A.; Schlexer, P.; Tosoni, S.; Pacchioni, G. Increasing Oxide Reducibility: The Role of Metal/Oxide Interfaces in the Formation of Oxygen Vacancies. *ACS Catalysis* **2017**, *7*, 6493–6513.
- (27) Greiner, M. T.; Chai, L.; Helander, M. G.; Tang, W.-M.; Lu, Z.-H. Transition Metal Oxide Work Functions: The Influence of Cation Oxidation State and Oxygen Vacancies. *Advanced Functional Materials* **2012**, *22*, 4557–4568.
- (28) Kauhler, J.; Chang, J.-H.; Whangbo, M.-H. Bonding and Oxidation State of a Transition Metal Atom Encapsulated in an Isolated Octahedral Cluster Cation of Main Group Elements: Synthesis, Crystal Structure, and Electronic Structure of Pt<sub>2</sub>In<sub>14</sub>Ga<sub>3</sub>O<sub>8</sub>F<sub>15</sub> Containing Highly Positive 18-Electron Complex [PtIn<sub>6</sub>]<sup>10+</sup> and Low-Valent In<sup>+</sup> Ions. *Journal of the American Chemical Society* **2005**, *127*, 2277–2284.
- (29) Saini, S.; Basera, P.; Arora, E.; Bhattacharya, S. Unraveling Thermodynamic Stability, Catalytic Activity, and Electronic Structure of [TM<sub>x</sub>Mg<sub>y</sub>O<sub>z</sub>]<sup>+ / 0 / -</sup>-Clusters at Realistic Conditions: A Hybrid DFT and ab Initio Thermodynamics Study. *The Journal of Physical Chemistry C* **2019**, *123*, 15495–15502.

- (30) Andersen, M.; Panosetti, C.; Reuter, K. A practical guide to surface kinetic monte carlo simulations. *Frontiers in chemistry* **2019**, *7*, 202.
- (31) Bhattacharya, A.; Bhattacharya, S. Exploring N-Rich Phases in  $\text{Li}_x\text{Ny}$  Clusters for Hydrogen Storage at Nanoscale. *The Journal of Physical Chemistry Letters* **2015**, *6*, 3726–3730.
- (32) Reetz, M. T.; Helbig, W. Size-Selective Synthesis of Nanostructured Transition Metal Clusters. *Journal of the American Chemical Society* **1994**, *116*, 7401–7402.
- (33) Bhattacharya, S.; Sonin, B. H.; Jumonville, C. J.; Ghiringhelli, L. M.; Marom, N. Computational design of nanoclusters by property-based genetic algorithms: Tuning the electronic properties of  $(\text{TiO}_2)_n$  clusters. *Phys. Rev. B* **2015**, *91*, 241115.
- (34) Soini, T. M.; Rsch, N. Size-dependent properties of transition metal clusters: from molecules to crystals and surfaces computational studies with the program ParaGauss. *Phys. Chem. Chem. Phys.* **2015**, *17*, 28463–28483.
- (35) Roduner, E. Size matters: why nanomaterials are different. *Chem. Soc. Rev.* **2006**, *35*, 583–592.
- (36) Li, L.; Larsen, A. H.; Romero, N. A.; Morozov, V. A.; Glinsvad, C.; Abild-Pedersen, F.; Greeley, J.; Jacobsen, K. W.; Nørskov, J. K. Investigation of Catalytic Finite-Size-Effects of Platinum Metal Clusters. *The Journal of Physical Chemistry Letters* **2013**, *4*, 222–226.
- (37) Rodriguez-Kessler, P. L.; Rodriguez-Domnguez, A. R. Stability of Ni Clusters and the Adsorption of  $\text{CH}_4$ : First-Principles Calculations. *The Journal of Physical Chemistry C* **2015**, *119*, 12378–12384.
- (38) Tasker, S. Z.; Standley, E. A.; Jamison, T. F. Recent advances in homogeneous nickel catalysis. *Nature* **2014**, *509*, 299–309.

- (39) Keim, W. Nickel: an element with wide application in industrial homogeneous catalysis. *Angewandte Chemie International Edition in English* **1990**, *29*, 235–244.
- (40) Monachino, E.; Greiner, M.; Knop-Gericke, A.; Schlogl, R.; Dri, C.; Vesselli, E.; Comelli, G. Reactivity of Carbon Dioxide on Nickel: Role of CO in the Competing Interplay between Oxygen and Graphene. *The Journal of Physical Chemistry Letters* **2014**, *5*, 1929–1934.
- (41) Bhattacharya, S.; Levchenko, S. V.; Ghiringhelli, L. M.; Scheffler, M. Efficient ab initio schemes for finding thermodynamically stable and metastable atomic structures: Benchmark of cascade genetic algorithms. *New Journal of Physics* **2014**, *16*, 123016.
- (42) Bhattacharya, S.; Levchenko, S. V.; Ghiringhelli, L. M.; Scheffler, M. Stability and metastability of clusters in a reactive atmosphere: Theoretical evidence for unexpected stoichiometries of  $Mg_MO_x$ . *Physical review letters* **2013**, *111*, 135501.
- (43) Bhattacharya, S.; Sonin, B. H.; Jumonville, C. J.; Ghiringhelli, L. M.; Marom, N. Computational design of nanoclusters by property-based genetic algorithms: Tuning the electronic properties of  $(TiO_2)_n$  clusters. *Physical Review B* **2015**, *91*, 241115.
- (44) Rogal, J.; Reuter, K. *Ab initio atomistic thermodynamics for surfaces: A primer*; 2006.
- (45) Arora, E.; Saini, S.; Basera, P.; Kumar, M.; Singh, A.; Bhattacharya, S. Elucidating the Role of Temperature and Pressure to the Thermodynamic Stability of Charged Defects in Complex Metal-Hydrides: A Case Study of  $NaAlH_4$ . *The Journal of Physical Chemistry C* **2019**, *123*, 62–69.
- (46) Hohenberg, P.; Kohn, W. Inhomogeneous Electron Gas. *Phys. Rev.* **1964**, *136*, B864–B871.
- (47) Kohn, W.; Sham, L. J. Self-Consistent Equations Including Exchange and Correlation Effects. *Phys. Rev.* **1965**, *140*, A1133–A1138.

- (48) Basera, P.; Saini, S.; Arora, E.; Singh, A.; Kumar, M.; Bhattacharya, S. Stability of non-metal dopants to tune the photo-absorption of TiO<sub>2</sub> at realistic temperatures and oxygen partial pressures: A hybrid DFT study. *Scientific reports* **2019**, *9*, 1–13.
- (49) Stuart, B. Infrared spectroscopy. *Kirk-Othmer Encyclopedia of Chemical Technology* **2000**,
- (50) Weng, W. Z.; Chen, M. S.; Yan, Q. G.; Wu, T. H.; Chao, Z. S.; Liao, Y. Y.; Wan, H. L. Mechanistic study of partial oxidation of methane to synthesis gas over supported rhodium and ruthenium catalysts using in situ time-resolved FTIR spectroscopy. *Catalysis today* **2000**, *63*, 317–326.
- (51) Sushkevich, V. L.; Verel, R.; van Bokhoven, J. A. Pathways of Methane Transformation over Copper-Exchanged Mordenite as Revealed by In Situ NMR and IR Spectroscopy. *Angewandte Chemie International Edition* **2020**, *59*, 910–918.
- (52) Fouladvand, S.; Skoglundh, M.; Carlsson, P.-A. A transient in situ infrared spectroscopy study on methane oxidation over supported Pt catalysts. *Catal. Sci. Technol.* **2014**, *4*, 3463–3473.
- (53) Wang, X.; Martin, N. M.; Nilsson, J.; Carlson, S.; Gustafson, J.; Skoglundh, M.; Carlsson, P.-A. Copper-modified zeolites and silica for conversion of methane to methanol. *Catalysts* **2018**, *8*, 545.
- (54) Ruiz-Franco, J.; Rovigatti, L.; Zaccarelli, E. On the effect of the thermostat in non-equilibrium molecular dynamics simulations. *The European Physical Journal E* **2018**, *41*, 80.
- (55) Perdew, J. P.; Burke, K.; Ernzerhof, M. Generalized Gradient Approximation Made Simple. *Phys. Rev. Lett.* **1996**, *77*, 3865–3868.

- (56) Saini, S.; Sarker, D.; Basera, P.; Levchenko, S. V.; Ghiringhelli, L. M.; Bhattacharya, S. Structure and electronic properties of transition-metal/Mg bimetallic clusters at realistic temperatures and oxygen partial pressures. *The Journal of Physical Chemistry C* **2018**, *122*, 16788–16794.
- (57) Heyd, J.; Scuseria, G. E.; Ernzerhof, M. Hybrid functionals based on a screened Coulomb potential. *The Journal of chemical physics* **2003**, *118*, 8207–8215.
- (58) Perdew, J. P.; Ernzerhof, M.; Burke, K. Rationale for mixing exact exchange with density functional approximations. *The Journal of chemical physics* **1996**, *105*, 9982–9985.
- (59) Blum, V.; Gehrke, R.; Hanke, F.; Havu, P.; Havu, V.; Ren, X.; Reuter, K.; Scheffler, M. Ab initio molecular simulations with numeric atom-centered orbitals. *Computer Physics Communications* **2009**, *180*, 2175 – 2196.
- (60) Lenthe, E. v.; Baerends, E. J.; Snijders, J. G. Relativistic regular twocomponent Hamiltonians. *The Journal of Chemical Physics* **1993**, *99*, 4597–4610.
- (61) Tkatchenko, A.; Scheffler, M. Accurate molecular van der Waals interactions from ground-state electron density and free-atom reference data. *Physical review letters* **2009**, *102*, 073005.
- (62) Martys, N. S.; Mountain, R. D. Velocity Verlet algorithm for dissipative-particle-dynamics-based models of suspensions. *Phys. Rev. E* **1999**, *59*, 3733–3736.
- (63) Evans, D. J.; Holian, B. L. The nose–hoover thermostat. *The Journal of chemical physics* **1985**, *83*, 4069–4074.

# Theoretical Insights into C–H Bond Activation of Methane by Transition Metal Clusters: The Role of Anharmonic Effects

Preeti Bhumla,\* Manish Kumar, and Saswata Bhattacharya\*

*Department of Physics, Indian Institute of Technology Delhi, New Delhi, India*

E-mail: Preeti.Bhumla@physics.iitd.ac.in[PB]; saswata@physics.iitd.ac.in[SB]

Phone: +91-11-2659 1359. Fax: +91-11-2658 2037

# Supplemental Material

- I.** Thermodynamic integration for Helmholtz free energy evaluation
- II.** Comparison of functionals (PBE and HSE06) in finding global minimum structures
- III.** Temperature control using Nose-Hoover thermostat



# I. Thermodynamic integration for Helmholtz free energy evaluation

We start from the fundamental relation between Helmholtz free energy  $F(T)$  and partition function  $Z$ .

$$F(T) = -k_B T \ln Z = -k_B T \ln \int e^{-\beta H} dp dr \quad (1)$$

where  $H$  (i.e., kinetic energy,  $K$ , plus potential energy,  $U$ ) is the Hamiltonian of the system (cluster), and  $\beta = 1/k_B T$ . This on integration gives us

$$F(T) = -k_B T \ln \int e^{-\beta U} dr + N k_B T \ln \Lambda(T) \quad (2)$$

where  $N$  is number of degrees of freedom and  $\Lambda(T)$  is the result of integration over momentum space and always valid only if the system is classical. In terms of  $\beta$ , the expression for  $\Lambda(\beta)$  is:  $\Lambda(\beta) = \sqrt{\frac{h^2 \beta}{2\pi m}}$

Equation 1 can then be written as:

$$\beta F(\beta) = -\ln \int e^{-\beta U} dr + N \ln \Lambda(\beta) \quad (3)$$

$$\frac{\partial[\beta F(\beta)]}{\partial \beta} = \frac{\frac{\partial}{\partial \beta} \int e^{-\beta U} dr}{\int e^{-\beta U} dr} + N \frac{\frac{\partial}{\partial \beta} \Lambda(\beta)}{\Lambda(\beta)} = \frac{\frac{\partial}{\partial \beta} \int e^{-\beta U} dr}{Z} + \frac{N}{2\beta} = \langle U \rangle_\beta + \frac{N}{2\beta} \quad (4)$$

$$\beta F(\beta) = \beta_\circ F(\beta_\circ) + \int_{\beta_\circ}^{\beta} \langle U \rangle_\beta d\beta + \frac{N}{2} \int_{\beta_\circ}^{\beta} \frac{\partial \beta}{\beta} \quad (5)$$

Now  $F(\beta_\circ)$  can be written as:

$$F(\beta_\circ) = \underbrace{E^{\text{DFT}} + U^{\text{ZPE}}}_{U^{\text{ref}}} + F^{\text{vib}}(\beta_\circ) \quad (6)$$

where from quantum approach, we have

$$F_{quantum}^{vib}(\beta) = \beta^{-1} \sum_{i=1}^N \ln(1 - e^{-\beta h \nu_i}) \quad (7)$$

and from classical approach, we have

$$F_{classic}^{vib}(\beta) = \beta^{-1} \sum_{i=1}^N \ln(\beta h \nu_i) \quad (8)$$

Therefore, we get the final expression of  $\beta F(\beta)$  as shown below:

$$\beta F(\beta) = \beta_o U^{ref} + \beta_o F^{vib}(\beta_o) + \int_{\beta_o}^{\beta} \langle U \rangle_{\beta} d\beta + \frac{N}{2} \ln \frac{\beta}{\beta_o} \quad (9)$$

We call the above equation as our master equation and we will approximate this equation as given below.

Here, we write  $\langle U \rangle_{\beta}$  as follows:

$$\langle U \rangle_{\beta} \rightarrow (\langle U \rangle_{\beta} - U^{ref}) \quad (10)$$

Therefore, on substituting this into Equation 9, we get

$$\beta F(\beta) = \beta_o U^{ref} + \beta_o F^{vib}(\beta_o) + (\beta - \beta_o) U^{ref} + \int_{\beta_o}^{\beta} (\langle U \rangle_{\beta} - U^{ref}) d\beta + \frac{N}{2} \ln \frac{\beta}{\beta_o} \quad (11)$$

$$= \beta U^{ref} + \beta_o F^{vib}(\beta_o) + \int_{\beta_o}^{\beta} (\langle U \rangle_{\beta} - U^{ref}) d\beta + \frac{N}{2} \ln \frac{\beta}{\beta_o} \quad (12)$$

This can be rewritten in terms of  $T=1/k_B\beta$  as follows:

$$F(T) = E^{DFT} + U^{ZPE} + \frac{T}{T_o} F^{vib}(T_o) - T \int_{T_o}^T \frac{dT}{T^2} (\langle U \rangle_T - U^{ref}) - k_B T \frac{N}{2} \ln \frac{T}{T_o} \quad (13)$$

## II. Comparison of functionals (PBE and HSE06) in finding global minimum structures

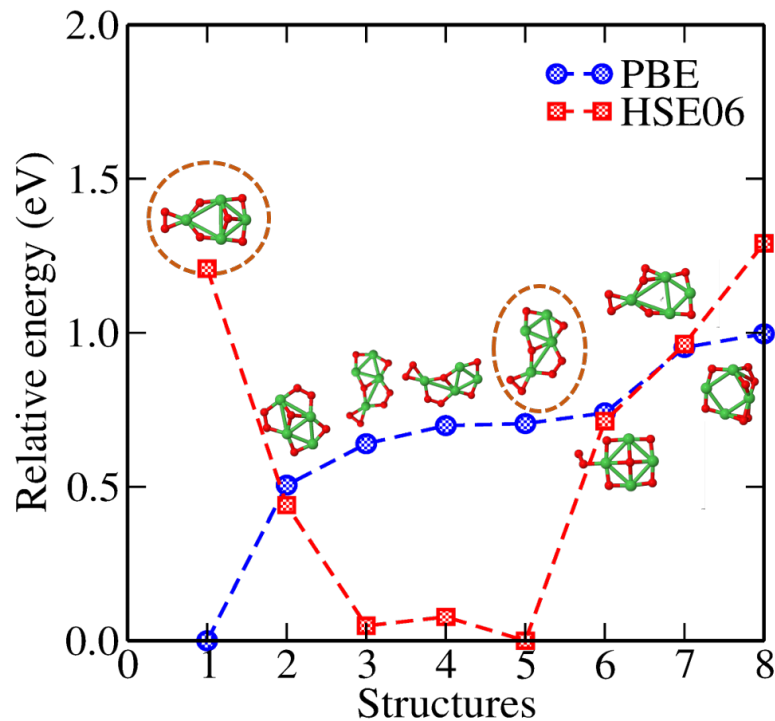


Figure S1: Structures of different isomers of Ni<sub>4</sub>O<sub>7</sub> clusters obtained from PBE (represented by dashed red line) and HSE06 (represented by dashed blue line) exchange-correlation ( $\epsilon_{xc}$ ) functionals. Dashed circles represent the global minima from the two functionals.



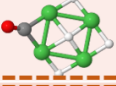
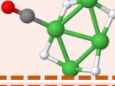
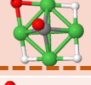
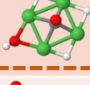
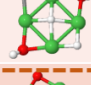
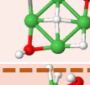
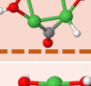
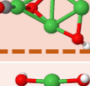
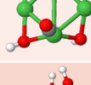
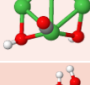
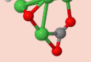
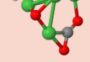
Clusters	PBE	HSE06
$\text{Ni}_4\text{CH}_4$		
$\text{Ni}_4\text{O}_1\text{CH}_4$		
$\text{Ni}_4\text{O}_2\text{CH}_4$		
$\text{Ni}_4\text{O}_3\text{CH}_4$		
$\text{Ni}_4\text{O}_4\text{CH}_4$		
$\text{Ni}_4\text{O}_5\text{CH}_4$		
$\text{Ni}_4\text{O}_6\text{CH}_4$		

Figure S2: Global minimum structures of  $\text{Ni}_4\text{O}_x\text{CH}_4$  clusters obtained from PBE and HSE06  $\epsilon_{xc}$  functionals. Dashed rectangle indicates the clusters having different global minima.

We have determined the energy of different isomers of  $\text{Ni}_4\text{O}_7$  clusters from both the  $\epsilon_{xc}$  functionals viz. PBE<sup>1</sup> and HSE06.<sup>2</sup> From Figure S1, we have found that PBE  $\epsilon_{xc}$  functional predicts structure 1 as the global minimum isomer while structure 5 is the global minimum isomer obtained from HSE06  $\epsilon_{xc}$  functional. Further, we have calculated the energy of  $\text{Ni}_4\text{O}_x\text{CH}_4$  ( $0 \leq x \leq 6$ ) series of clusters from PBE as well as HSE06  $\epsilon_{xc}$  functionals (see Figure S2). We have noticed different trends of energy from both functionals. For  $\text{Ni}_4\text{O}_1\text{CH}_4$ ,  $\text{Ni}_4\text{O}_2\text{CH}_4$  and  $\text{Ni}_4\text{O}_4\text{CH}_4$  clusters, PBE and HSE06  $\epsilon_{xc}$  functionals predict different global minimum structures. As it is already well established that for oxygen molecule, HSE06 being advanced functional gives correct binding energy,<sup>3</sup> therefore, we have chosen HSE06 for our oxide based clusters.

### III. Temperature control using Nose-Hoover thermostat

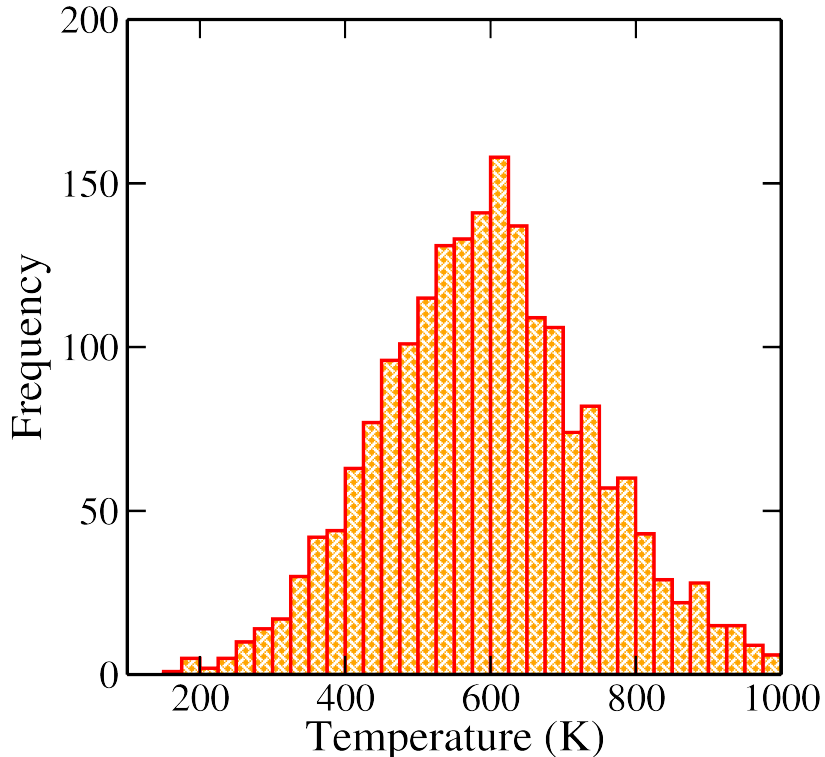


Figure S3: Histogram of *aiMD* simulation for  $\text{Ni}_4\text{O}_6\text{CH}_4$  cluster at  $T = 600$  K.

Here, we represent a test case of  $\text{Ni}_4\text{O}_x(\text{CH}_4)_y$  cluster to validate our *ab initio* molecular dynamics (*aiMD*) simulations. We have carried out *aiMD* simulations at five different temperatures in canonical ensemble with time and time-step being 8 ps and 1 fs, respectively. Temperature control is realized by employing the Nose-Hoover thermostat.<sup>4</sup> Figure S3 shows the histogram that we have obtained from *aiMD* simulation for  $\text{Ni}_4\text{O}_6\text{CH}_4$  cluster at  $T = 600$  K. From the histogram, we infer that average temperature of the simulation is indeed coming around the intended temperature viz. 600 K. Note that here, only the last 1 ps equilibrium stable data is considered after ignoring a large part of the data to avoid any thermal fluctuations. Therefore, Nose-Hoover thermostat is apt to control the temperature during simulation.

## References

- (1) Perdew, J. P.; Burke, K.; Ernzerhof, M. Generalized gradient approximation made simple. *Phys. Rev. Lett.* **1996**, *77*, 3865.
- (2) Heyd, J.; Scuseria, G. E.; Ernzerhof, M. Hybrid functionals based on a screened Coulomb potential. *The Journal of chemical physics* **2003**, *118*, 8207–8215.
- (3) Bhattacharya, S.; Levchenko, S. V.; Ghiringhelli, L. M.; Scheffler, M. Stability and metastability of clusters in a reactive atmosphere: Theoretical evidence for unexpected stoichiometries of  $\text{Mg}_M\text{O}_x$ . *Physical review letters* **2013**, *111*, 135501.
- (4) Evans, D. J.; Holian, B. L. The nose–hoover thermostat. *The Journal of chemical physics* **1985**, *83*, 4069–4074.